ANNUAL REVIEWS

Annual Review of Physical Chemistry

Droplet Interfacial Tensions and Phase Transitions Measured in Microfluidic Channels

Priyatanu Roy,[1] Shihao Liu,[1] and Cari S. Dutcher[1,2]

[1]Department of Mechanical Engineering, University of Minnesota, Twin Cities, Minneapolis, Minnesota 55455, USA; email: cdutcher@umn.edu

[2]Department of Chemical Engineering and Materials Science, University of Minnesota, Twin Cities, Minneapolis, Minnesota 55455, USA

Annu. Rev. Phys. Chem. 2021. 72:73–97

First published as a Review in Advance on February 19, 2021

The *Annual Review of Physical Chemistry* is online at physchem.annualreviews.org

https://doi.org/10.1146/annurev-physchem-090419-105522

Keywords

microfluidics, interfacial tension, phase transitions, aerosols, emulsions, droplets

Abstract

Measurements of droplet phase and interfacial tension (IFT) are important in the fields of atmospheric aerosols and emulsion science. Bulk macroscale property measurements with similar constituents cannot capture the effect of microscopic length scales and highly curved surfaces on the transport characteristics and heterogeneous chemistry typical in these applications. Instead, microscale droplet measurements ensure properties are measured at the relevant length scale. With recent advances in microfluidics, customized multiphase fluid flows can be created in channels for the manipulation and observation of microscale droplets in an enclosed setting without the need for large and expensive control systems. In this review, we discuss the applications of different physical principles at the microscale and corresponding microfluidic approaches for the measurement of droplet phase state, viscosity, and IFT.

1. INTRODUCTION

LLPS: liquid–liquid phase separation

Measurements of the physical properties of fluids are traditionally done in bulk with large sample volumes. Recent advances in droplet generation, manipulation, and observation techniques have extended these measurements to micrometer length scales (1, 2). This microscopic-length scale becomes relevant in complex and multiphase fluid systems such as aerosols, emulsions, suspensions, and biological fluidic mixtures, in which the measurement of bulk fluids is often not feasible due either to the lack of substantial sample volumes or to the small characteristic length scales governing the dynamics of the system. For example, atmospheric aerosol particles and droplets fall into both categories: Their sample volumes are often extremely limited and their characteristic length scales range from micrometers to nanometers (3). These chemically complex small droplets and particles are ubiquitous in our environment and have a large effect on the climate by moderating Earth's albedo, both directly by solar scattering and absorption and indirectly by forming clouds (3). Predictive modeling of these effects requires precise knowledge of the chemical and physical properties of individual aerosol particles such as their surface tension (4), viscosity (5), and phase [including phase transitions such as ice nucleation and liquid–liquid phase separation (LLPS)] (6, 7). For accurate measurements, shrinking down bulk measurement techniques is often necessary to observe isolated single (8) or multiple particles at the relevant length scales (9).

Microfluidic devices are a special class of liquid flow channels with micrometer length scales in one or more directions and are usually fabricated in some transparent material for optical observation. These devices are used extensively in biomedical (10), industrial (11), and environmental (12) monitoring applications as well as in fundamental research on multiphase systems such as emulsions (13, 14) and aerosols (15). The advantages of such small length scales and confined geometry include shorter thermal and material transport length scales, which allow access to flow regimes usually not accessible in bulk-scale experiments. Additionally, the small sample volume required, the ease of design, and the affordable manufacturing cost of these devices make them ideal for applications in which the sample is much rarer and more precious than the sampling equipment.

In the following sections, we review methods for measuring the phase state, viscosity, and surface tension of single particles at the microscale. The review is organized by the physical principle of droplet measurement into different sections as shown in **Figure 1** with measurements performed with microscale procedures and their corresponding microfluidic-based equivalent approaches for high-throughput or multiplexed data collection. First, measurements on sessile drops on a solid substrate are discussed, in which imaging techniques are used to measure the phase state or viscosity of the droplets (**Figure 1*a***). Second, force tensiometry methods in which droplet curvature or overall distortion from circularity is used to infer surface tension and viscosity are discussed (**Figure 1*b***). Third, droplet oscillations in which the physical properties are calculated from the oscillation frequency and amplitude are discussed (**Figure 1*c***). Finally, we discuss some deflection-based methods in which external probes are used for physical property measurements (**Figure 1*d***).

2. MEASURING DROPLET PROPERTIES AT THE MICROSCALE

2.1. Optical-Based Microscale Methods for Phase and Viscosity Measurements

One of the simplest ways to infer the phase and viscosity of a droplet is by depositing it on a surface and observing it over time. Optical microscopy–based methods can be performed without probes or with microscopic particles immersed inside the droplet used as probes, both on static stages and in microchannel devices.

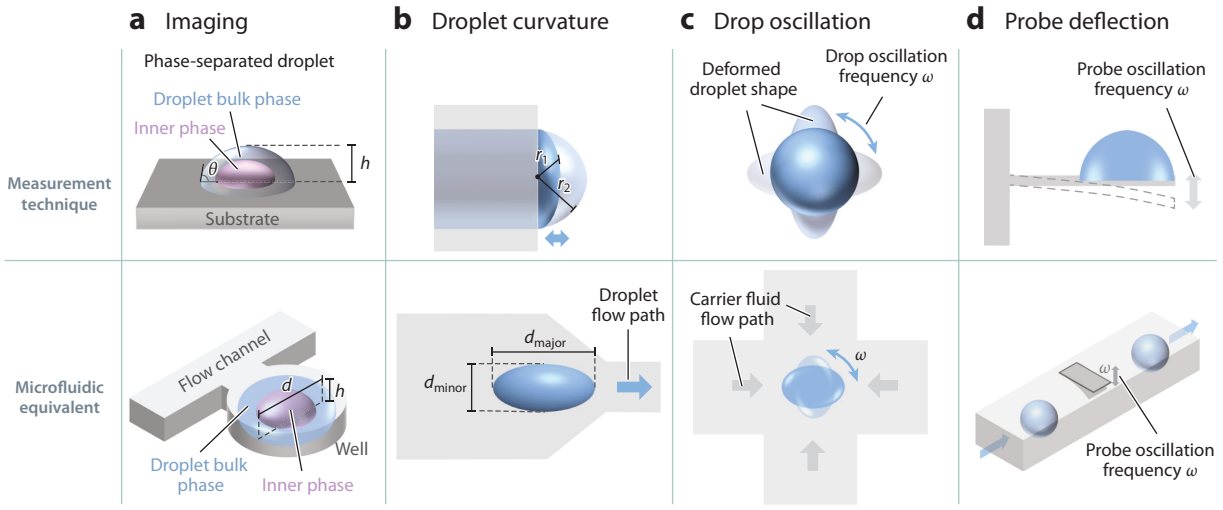

Figure 1

(*Top row*) Surface tension and phase measurement principles at the microscale including (*a*) imaging-based, (*b*) droplet curvature– or overall shape–based, (*c*) drop oscillation–based, and (*d*) probe deflection–based methods. (*Bottom row*) Representative equivalent microfluidic setups. θ, d, and h are the droplet contact angle, diameter, and height, respectively, for imaging-based methods. r_1 and r_2 are the droplet radii corresponding to different upstream pressures. d_{major} and d_{minor} are the major and minor axes of a deformed droplet as it enters a microfluidic constriction during surface/interfacial tension measurement for droplet curvature–based methods. ω refers to oscillation frequency of either the droplet or a probe in drop oscillation– and probe deflection–based methods.

2.1.1. Single droplets without immersed probes. Experiments on droplets can be conducted in an environmental cell in which the temperature of the substrate is controlled from the bottom and a stream of relative humidity (RH)-controlled air is flowed over the droplet. Usually the substrate is coated with a hydrophobic layer to minimize the impact of the surface free energy of the solid surface on the phase transitions of the droplet. Particle outlines as well as inner features are monitored to determine if the droplet is completely mixed, phase separated, or effloresced (16–18) and to explore supersaturated and supercooled states not readily accessible at the macroscale. Using a Raman spectroscope, droplet chemistry can be probed, thus revealing additional chemical information about particles not evident from simple optical microscopy (**Figure 2*a*,*b***). For example, in efflorescence experiments, Raman spectra show that the rate of RH change (19) as well as the actual temperature of efflorescence (20) can affect the crystal structure in sea salt aerosols and NaCl droplets. This Raman environmental microscopy approach, which is shown in **Figure 2*a*,*b***, has proved especially popular in ice nucleation studies (21–24) that evaluate the impact of soluble or insoluble ice nucleating particles (INPs) present in an aqueous droplet on its ice nucleation temperature.

2.1.2. Single droplets with immersed probes. Optical experiments can be augmented with fluorescence-labeled imaging to assist in the detection of phase separation and the surface chemistry of droplets under different ambient conditions (25). The quantitative measurement of phase transitions in droplets can also be expressed by changes in viscosity. For example, fluorescent probes have been used for real-time viscosity measurements of particle decay and oxidative aging using fluorescence lifetime imaging techniques in secondary organic aerosols (26). Another approach consists of quantification of the internal flow field of a droplet with or without an external perturbation, thus providing a measurement of the viscosity. Particle-tracking microrheology (27)

RH: relative humidity

INP: ice nucleating particle

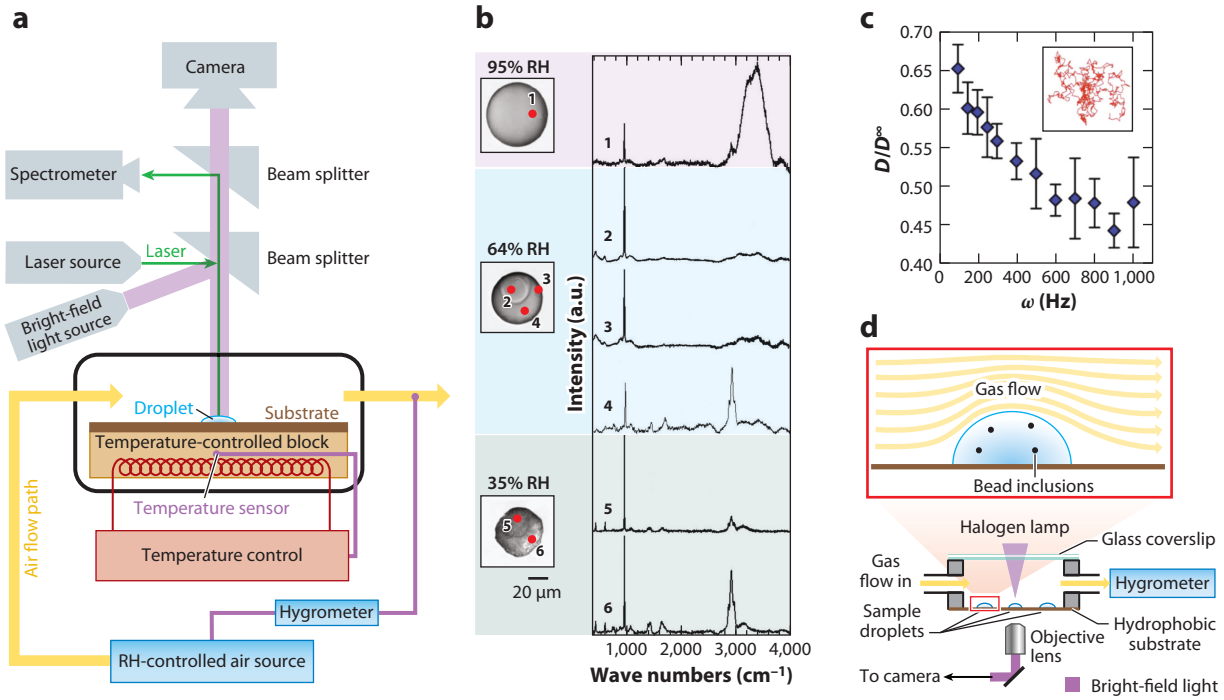

Figure 2

(*a*) Illustration showing an environmental cell microscopy setup with a Raman spectroscope. (*b*) Spectra and photographs showing liquid–liquid phase separation in an aqueous solution of multiple dicarboxylic acids with six carbon atoms and ammonium sulfate and the corresponding Raman spectra of phases at different relative humidities (RHs). The spectra shown are taken at the locations in the droplets shown by the corresponding numbers. Panel *b* adapted from Reference 18 (CC BY-SA 3.0). (*c*) Graph illustrating an example of particle tracking for calculating diffusivity. The inset shows a representative particle trajectory over a 10 × 10 micrometer grid. Panel *c* adapted with permission from Reference 28; copyright 2013 American Physical Society. (*d*) An illustration of the bead mobility technique employed in droplets deposited on a substrate subjected to a steady stream of directed gas flow. Panel *d* adapted from Reference 30 (CC BY-SA 3.0).

is an example of this technique, in which fluorescent particles are dispersed in a droplet and imaged with a video camera (**Figure 2*c***). Software can be used to track each particle, and the viscosity of the fluid (μ) is estimated from the 3D Brownian motion of the particles in the Stokes regime using the equations

$$\mu = \frac{kT}{6\pi D r_p} \quad \text{and} \quad \langle x^2 \rangle = 6Dt, \qquad 1.$$

where r_p is the probe particle radius, D is the diffusivity of the particle in the droplet phase, k is the Boltzmann constant, T is the temperature, and $\langle x^2 \rangle$ is the mean squared displacement of the particle over observation period t. **Figure 2*c*** shows the calculated diffusivities using this technique alongside the path taken by a single particle to determine the diffusivity of particles near a solid surface (28). In some cases, the method has been improved with the use of an external force gradient added by using magnetic probe particles and a magnetic field (29). A bead-mobility technique (30) has also been proposed that uses an external flow of gas to drive particles inside a droplet using shear stresses (**Figure 2*d***) and then tracks their motion.

2.1.3. Droplet phase transitions using microfluidics. Microfluidics can also be used in place of substrate-based methods, allowing the droplet's internal mixing state to be investigated without the need for an environmental cell. Devices for this application consist of a droplet-generation section, flow channels, and arrays of traps. The simplest microfluidic devices are usually constructed by imprinting or etching a rectangular cross section into an optically transparent flat substrate and subsequently being sealed to another flat substrate. The device usually has multiple inlet and outlet ports providing access to external tubing that connects to pumps or reservoirs for access to fluid flow. The types of microfluidic devices and microfabrication processes (31) depend on the geometric requirements, channel wall surface chemistry, and device mechanical properties.

PDMS: poly(dimethylsiloxane)

EWOD: electrowetting on dielectric

For studies of droplet phase transition, poly(dimethylsiloxane) (PDMS) (32) devices offer an advantage over other materials such as poly(methyl methacrylate), glass, or Teflon™. In addition to being inexpensive and easy to use, PDMS is slightly permeable to water and impermeable to most dissolved organic molecules or salts (33). The driving force for water pervaporation to or from the trapped droplet is the osmotic pressure across the PDMS layer. This property of PDMS precludes the need for external RH control, as the chemical potential of water in the droplet slowly equilibrates with the RH external to the microfluidic device, starting from a saturated state. Samples can be loaded on chips and droplets can be generated and isolated in individual wells (**Figure 3*a***) to allow the tracking of changes in phase over time. Experimental images of a well-mixed aqueous solution of multiple salts and 3-methylglutaric acid crystallizing and phase separating over the course of an experiment are shown in **Figure 3*c*** (34).

This single layer well design is the most widely used trap geometry (34–41). Modifications of this simple design include additional layers for varying purposes. Multilayer designs include ones where the well sits at a different height from the main flow channel to assist in droplet capture (42–45). The layers can also be used for providing additional paths for water exchange by changing the chemical potential gradient experienced by the trapped droplet through the use of multiple reservoirs (44) as shown in **Figure 3*d***. These devices provide control over droplet dehydration/rehydration as well as the corresponding rates as shown in **Figure 3*e***. Devices with droplets coated in oil but without a PDMS layer have also been used (46, 47). Microevaporation-based approaches with a single initial phase of liquid without a carrier phase by precise pumping to control the evaporation rate have also been used (48, 49). Flow-through approaches are also common where either droplets (50) or slugs of liquid (51–53) change phase rapidly while moving in a channel due to the thermodynamic conditions of the system. Other studies have employed co-flow-based systems in which the position of the interface determines the phase equilibrium (54, 55). An innovative device design utilized a 2D array of cells with temperature and pressure gradients to visualize the thermodynamic phase diagram in the two-phase region (56, 57). Massive arrays of droplets have also been used to gather statistically significant data in a short amount of time (44, 58, 59). These devices have been used in the past to study protein crystallization kinetics (60), protein phase separation (52), polymer and salt phase boundary exploration (44), salt crystallization kinetics (48), ice nucleation temperature determination (47, 59) and atmospheric aerosol liquid-liquid phase separation and efflorescence (34, 40). However, while these approaches provide an estimation of the droplet phase state in a multicomponent system, there is another class of microfluidic devices discussed later which are used for measuring viscosity, used in aerosol science as a proxy of the phase (sometimes binned into "solid," "semisolid," and "liquid" categories).

Finally, the field of digital microfluidics (61, 62) can also be used to manipulate droplets in a controlled manner, often with electric or magnetic fields. Already, digital microfluidics is widely used for mixing, chemical analysis, and biological assays; however, it can also be adapted to probe droplet physical properties. Individual droplets are moved on a substrate using the magneto- or electrowetting on dielectric (EWOD) principle in a device with a two-plate or

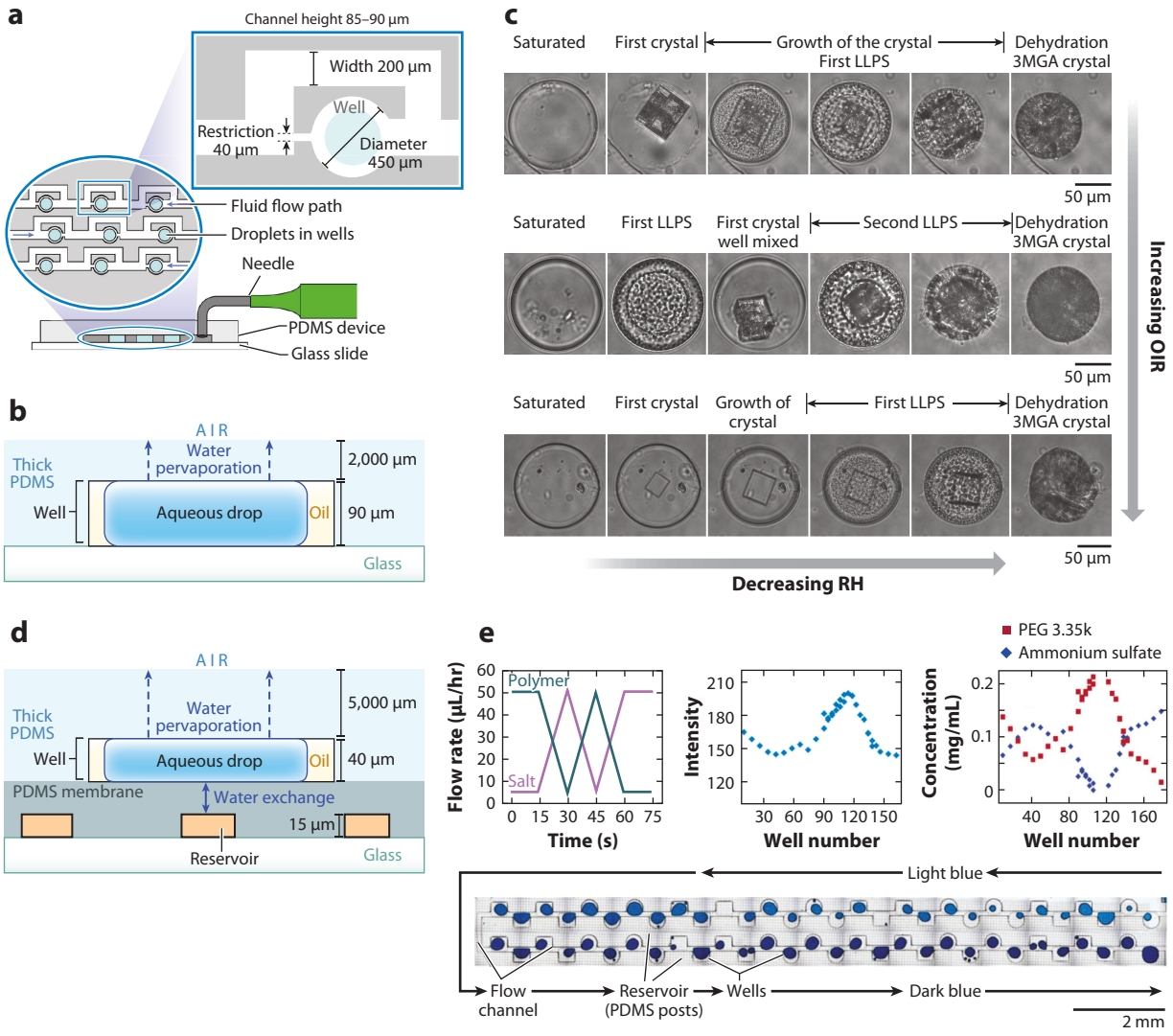

Figure 3

(*a*) A schematic showing (*top*) a microfluidic static well used for trapping and studying single droplets during dehydration and (*bottom*) the droplet loading process in a multiwell device. (*b*) A cross-sectional schematic of the microfluidic device showing the trapped droplet and water pervaporation path. (*c*) Photographs of phase transitions observed in droplets with 3MGA, NaCl, and $MgCl_2$ under constantly reducing RH shown for different OIRs. Panels *a*, *b*, and *c* adapted with permission from Reference 34; copyright 2019 American Chemical Society. (*d*) A cross-sectional schematic of a multistep microfluidic device for external control of the drying rates of droplets. The primary thick PDMS layer on the top contains the droplet wells and a secondary thinner PDMS membrane layer on the bottom contains reservoirs for water exchange with the wells. (*e*) Graphs showing the creation and storage of a population of droplets containing a polymer (PEG 3.35k) and ammonium sulfate as well as solute concentration measurements using the color intensity of droplets labeled with a blue dye. (*Left*) Droplet formation by co-flowing PEG and ammonium sulfate solutions in alternate pulses. (*Middle*) Light transmittance of stored droplets in different wells on the same microfluidic chip. (*Right*) Concentration of the phases in droplets stored in different wells. (*Bottom*) Photograph showing solution droplets trapped in wells and a large water-exchange reservoir underneath supported by PDMS posts. Panels *d* and *e* adapted with permission from Reference 44; copyright 2007 American Chemical Society. Abbreviations: 3MGA, 3-methylglutaric acid; LLPS, liquid–liquid phase separation; OIR, organic-to-inorganic ratio; PDMS, poly(dimethylsiloxane); PEG, polyethylene glycol; RH, relative humidity.

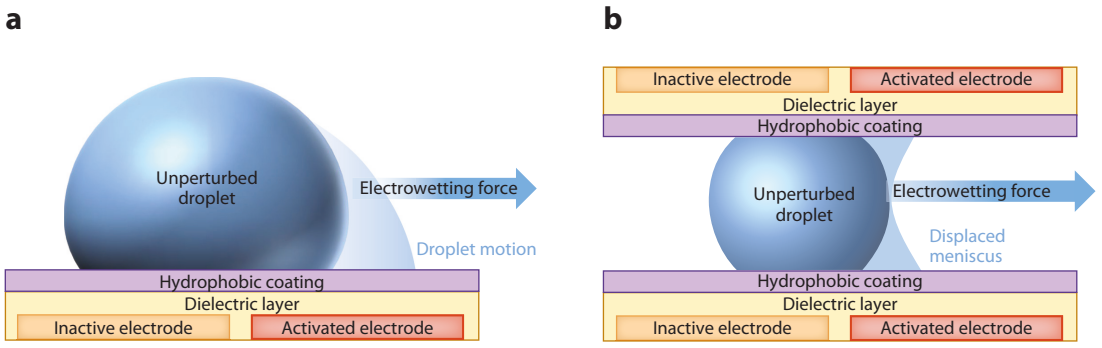

Figure 4

Schematic illustrations of digital microfluidic devices based on the electrowetting on dielectric (EWOD) principle. (*a*) One-plate or open-ended EWOD devices can be used for transporting droplets with the coordinated activation of electrodes. The droplet sits on a hydrophobic coated dielectric substrate with the electrodes embedded inside. (*b*) Two-plate or closed devices can also be used for this purpose. However, observation of droplet motion is more difficult in closed devices. Changes in pressure in both sides of the droplet can be used as an indicator of droplet meniscus motion, as described in Reference 64.

open-ended configuration (**Figure 4**). The substrate is usually coated in a precise pattern of thin-film electrodes that are used to generate the attractive or repulsive forces for the droplets. Viscosity (63, 64) and interfacial tension (IFT) (65) between two liquid phases have been measured in these devices. Tröls et al. (64) used a two-plate device to study the meniscus motion of a droplet under electrowetting forces. Electrodes in the substrate were used to pull the droplet meniscus combined with pressure sensors on either end to detect the meniscus displacement. When calibrated with liquids of known viscosity, microliter-sized test droplet viscosities could be measured. Digital microfluidics can also be applied to study droplet evaporation rates (66) or to prepare phase-separated droplets for further study (67).

2.1.4. Freezing and ice nucleation measurements using microfluidics. Many of the measurements discussed in the previous section are performed at room temperature. However, temperature control can be readily incorporated using environmental chambers or on-chip controls. For atmospheric aerosols, understanding the ice nucleation temperatures of particles is of key importance for climate modeling. Two characteristics of INP studies are the collection of a large quantity of droplet data and the precise knowledge of ice nucleation temperature. Conventional ice nucleation measurements include continuous flow diffusion chambers (68), cloud expansion chambers (69), ice spectrometers (70), environmental cell Raman microscopes (20), and droplets on substrate methods ranging from droplet volumes of picoliters (71) to microliters (72), as mentioned in Section 2.1.1. While these methods have shown the feasibility of the measurements, microfluidics offers the unique advantages of potentially high-throughput, contactless measurements and simpler devices, thus enabling more accurate and repeatable data collection.

IFT: interfacial tension

Microfluidic devices for studying INPs use two distinct approaches: static and flow-through. The two approaches differ in how droplet generation and freezing are performed. In a static device, a microfluidic monodispersed droplet generator can be used, as described by Riechers et al. (73) and Tarn et al. (74), to collect droplets in a microcentrifuge tube before placing the droplets in a monolayer on a cold plate for a temperature sweep. **Figure 5*a*** shows the droplet generation and storage as well as the droplet freezing and the ice nucleation temperature measurement of ultrapure water in this type of setup. Another static INP device used by Brubaker et al. (59) is similar to the microfluidic phase-separation studies described in Section 2.1.3. In such a device, a

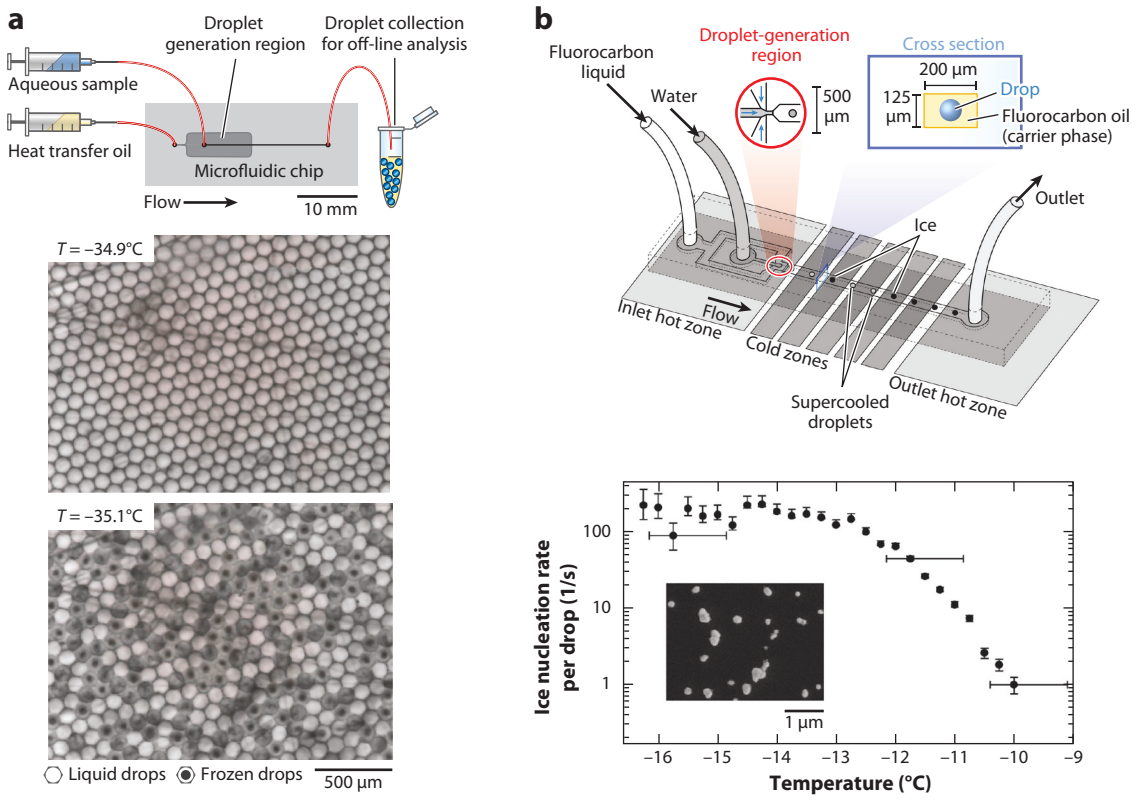

Figure 5

(*a*) Schematic and photographs showing ice nucleation in a static device. (*Top*) Droplet generation in a microfluidic chip and collection in a microcentrifuge tube; (*middle*) droplet freezing experiments for a monolayer of ultrapure water droplets on a cold stage showing all liquid drops in bright color; and (*bottom*) liquid and frozen drops, the latter indicated by bright drops with a dark center. Panel *a* adapted from Reference 74 (CC BY-SA 4.0). (*b*) Illustration showing a flow-through device for high-throughput ice nucleating particle detection. (*Top*) A device schematic showing the microfluidic droplet-generation region, the flow channel, and the multiple cold zones and (*bottom*) a graph of an ice nucleation temperature spectrum for silver iodide nanoparticles in water. The inset shows a scanning electron microscope image of the nanoparticles after synthesis. Panel *b* adapted with permission from Reference 75; copyright 2009 The Royal Society of Chemistry.

large array of static traps is used to generate the droplets on-chip and then the trapped droplets are frozen in place. In both cases, the onset of freezing is detected using a change in droplet optical intensity as the ice crystals start to grow.

In the flow-through approach for generating large data sets in a quick amount of time, which has been used by Stan et al. (75), droplets were generated on-chip and flown through a channel before being extracted at the chip outlet. The researchers used a highly tunable temperature gradient along the flow channel length. As a result, the droplets experienced a specific cooling rate while flowing through the channel before freezing at any given point. The freezing location could be correlated to the freezing temperature due to the aforementioned temperature gradient. In this case, on-chip thin film platinum resistive temperature sensors were also used to ensure that the measured temperature was highly accurate and specific to the location being measured. **Figure 5*b*** shows the microfluidic channel and the cold stage for this measurement. This device was used for measuring the ice nucleation temperature of pure water (homogeneous ice nucleation) and silver

iodide (heterogeneous immersion–mode ice nucleation) (**Figure 5*b***) and comparing the results with other methods (75).

2.2. Droplet Curvature– or Shape Deformation–Based Interfacial Tension Measurement

Surface (liquid–vapor) or interfacial (liquid–liquid) tension of a droplet can be measured directly or indirectly by combining measures of droplet shape or curvature with local equilibrium force or energy balances. This is the most widely used family of methods for measurement of IFT in pure (or so-called neat) systems as well as systems with surface-active species such as surfactants. Microscale and microfluidic methods for studying curvature-dependent thermodynamic equilibrium properties and dynamic surface adsorption kinetics of both neat and complex interfaces are described in this section.

2.2.1. Pressure-based tensiometry (pressure–capillary). The most common of these shape-based methods utilizes excess capillary pressure created by a curved surface or interface to measure IFT, using the well-known Young-Laplace equation (76) to calculate the pressure difference ΔP across the interface,

$$\Delta P = \gamma \left(\frac{1}{r_1} + \frac{1}{r_2} \right), \qquad 2.$$

where r_1 and r_2 are the radii of curvature of the interface in two perpendicular directions and γ is the IFT. Due to the IFT, the pressure is higher on the inside of a curved interface than it is on the outside, and that pressure difference can be measured using pressure probes on either side of the interface.

One of the simplest applications of this principle is used in maximum bubble pressure–based tensiometers (77, 78), which are widely available as commercial instruments. Usually a highly accurate pressure sensor is required for this type of measurement. The maximum pressure to create a gas bubble in a liquid from a capillary is correlated with the capillary diameter to calculate the IFT. Variations of this method include capillary rise in a tube and drop volume or weight measurement. Both methods use the Young-Laplace pressure force balanced with gravitational force to measure the IFT; setups for these methods are widely available commercially as well. Microtensiometry with bubble pressure–based tensiometers has also been developed (79), as shown in **Figure 6*a***. This is similar to the maximum bubble pressure method except that the droplet curvature is assessed with the pressure. Another method using micropipettes to image the interface curvature internal to a glass capillary under a known pressure difference has also found wide use (80).

Microfluidic devices have also been designed to measure IFT using this principle. Because the microchannels are commonly made from PDMS and glass, the contact angles and hence the radii of curvature from Equation 2 are also affected by the wettability of these materials. Tapered channels were used in a study (81) (**Figure 6*b***) that correlated the radii of the curvature in the horizontal (viewing) plane, r_h, and vertical (cross-sectional) plane, r_v, of the interface to the location of the interface along the tapered channel using the formula

$$\Delta P = \gamma \left(\frac{1}{r_h} + \frac{1}{r_v} \right) = \gamma \left(\frac{-2\cos\theta}{h} + \frac{-2\cos(\theta - \alpha)}{W_{min} + 2x\tan\alpha} \right), \qquad 3.$$

where θ is the average contact angle with the top and bottom of the channel, h is the height of the channel (constant everywhere), W_{min} is the minimum width of the tapered channel, x is the distance of the interface from the opening, and α is the half-taper angle. With the axial location of the interface identified, the IFT can be determined using Equation 3. However, this method

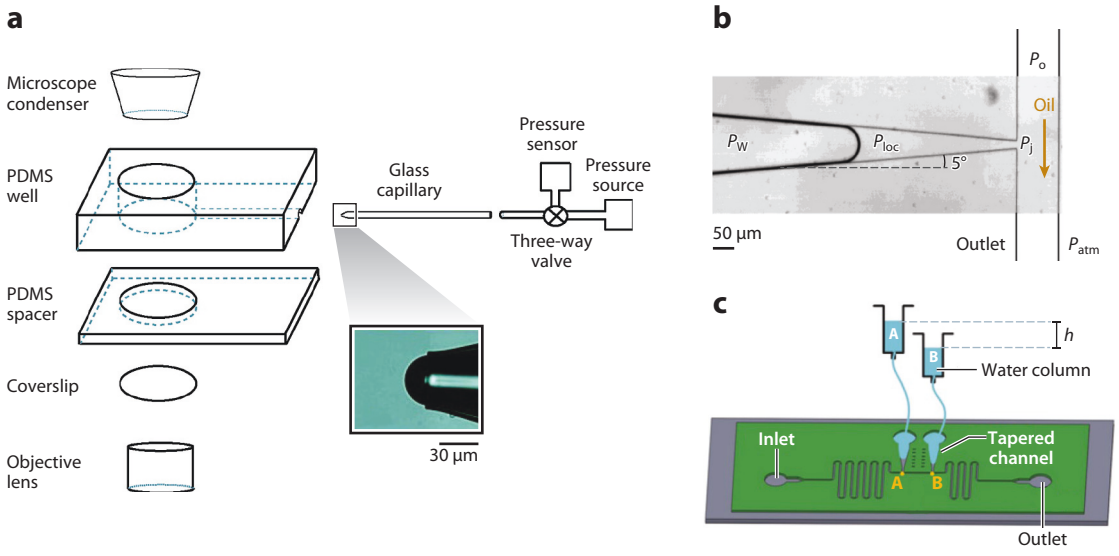

Figure 6

(*a*) Schematic showing a microtensiometer using a glass capillary for droplet generation (see photograph) and an imaging system to track droplet curvature as a function of pressure. Panel *a* adapted with permission from Reference 79; copyright 2010 American Chemical Society. (*b*) A photograph showing a tapered microfluidic channel using the Young-Laplace principle to measure interfacial tension. *P* refers to pressure and the subscripts "o," "w," "loc," and "j" refer to oil, water, local, and junction, respectively. Panel *b* adapted with permission from Reference 81; copyright 2011 Elsevier Science. (*c*) An illustration of a two-channel device that eliminates the need for a precise pressure measurement, as the pressure difference between points A and B can be calculated from the difference between the static pressure heads of the reservoirs. This can be done by adjusting the reservoir heights until the interfaces line up at the same location in the two tapered channels. Panel *c* adapted with permission from Reference 82; copyright 2013 AIP Publishing. Abbreviation: PDMS, poly(dimethylsiloxane).

still requires the precise measurement of pressure using external sensors to calculate the IFT accurately. Another study (82) eliminated this requirement with a pair of tapered microfluidic channels (**Figure 6*c***) in which the pressure difference measurement can be made in two steps: first, by adjusting the equilibrating static pressure head of the two channels and measuring the curvature of the interfaces located at different positions inside the taper, and second, by comparing the water column height difference between the channels when the interfaces are brought to the same location in the taper. There are a number of other microfluidic applications of the Young-Laplace equation for IFT measurements, including droplet generation from an array of micropores (83), from a micropipette inside a microfluidic channel (84), and from a single capillary tube inside a microfluidic channel (85).

2.2.2. Spinning drop tensiometry (inertia–capillary). While straightforward, Young-Laplace-based measurements that relate pressure drop to the radius of curvature become challenging at the limit of ultralow IFT (<1 mN/m) or high Bond number (*Bo*, equal to the ratio of gravitational to capillary forces), which are typically encountered in the areas of petroleum refining, surfactant-laden emulsion systems, and biolipid interfaces. The limitation arises from the accuracy of the pressure measurement or the curvature determination of droplets at low IFT. Instead, another force such as inertia can be balanced with capillary forces. An example is spinning drop tensiometry, in which a liquid drop or bubble suspended in another liquid is spun around at a high angular velocity inside a capillary tube and the resulting ellipsoid- or cylinder-shaped

droplet is imaged. The IFT is then given by the equation (86)

$$\gamma = \frac{1}{4} r_d^3 \Delta\rho\omega^2, \quad 4.$$

where $\Delta\rho$ is the density difference between the droplet and the continuous phase, r_d is the distorted droplet radius, and ω is the angular velocity. This method can determine IFT down to 10^{-6} mN/m.

2.2.3. Droplet shape–based tensiometry (gravity–capillary). While not typically thought of as a microscale measurement, it is worth briefly mentioning the well-known pendant drop method, which uses droplet shape analysis to get curvature data to infer the IFT (87). In this method, a drop suspended from a capillary distorts from its usual perfectly spherical shape due to the combined effect of gravity pulling on the droplet and the IFT trying to restore the equilibrium spherical shape. Likewise, sessile drop shape analysis can be performed by placing the droplet on a substrate and measuring the contact angles (**Figure 1*a***). Pendant drop measurements can be taken down to droplet sizes of ∼0.2 mm (88). No pressure measurement across the droplet interface is required, and consequently shape-based methods have found wide use in droplet microfluidic approaches for tensiometry (with deforming forces from flow instead of gravity), which are discussed next.

2.2.4. Droplet-generation tensiometry using microfluidics. Droplet generation (89) itself can be used as the basis of IFT measurement. Usually, two immiscible fluids are required, the dispersed phase and the continuous phase. They flow into the device through different inlets and meet at certain junctions where droplets and bubbles pinch off from the dispersed phase due to the enhanced interfacial stabilities from the local flow field deforming the interface. Typical designs of the junctions include T-junction, co-flowing, and flow-focusing geometries (90), as shown in **Figure 7*a–c***.

Nguyen et al. (91) measured the surface tension of aqueous solutions with varying concentrations of the ionic surfactant cetyl trimethyl ammonium bromide by introducing an optical sensor downstream of a T-junction (**Figure 7*a***) to detect the bubble-generation frequency. The varying laser intensity due to the generated air bubbles was recorded as pulses indicating the bubble-generation frequency. With assumptions such as steady flow; negligible inertia, momentum, and buoyancy force; and Marangoni effect, a relationship between formation frequency and surface tension was proposed based on the force balance of tension and drag force,

$$f = \frac{3\alpha W_c^2 \rho_c^{\frac{3}{2}} \overline{u_c}^4}{16(C_s W_d / C_D)^{\frac{3}{2}} \gamma^{\frac{3}{2}}}, \quad 5.$$

where f is bubble-formation frequency; α is the flow rate ratio of air to continuous phase; W_c is the diameter of the continuous phase channel; ρ_c is the density of continuous phase; $\overline{u_c}$ is the average velocity of the continuous phase; C_s and C_D are coefficients for the surface tension and drag forces, respectively; and W_d is the diameter of the dispersed phase channel.

Xu et al. (92) likewise developed a tensiometer in a coaxial microfluidic device (**Figure 7*b***) to measure the IFT of water phase dispersed into oil phase. Here, the force balance in the droplet-dripping regime between the viscous force and tension force was established to calculate the IFT using the equation

$$\gamma = \frac{k_D(\overline{u_c} - \overline{u_d})\mu_c d^2}{\pi W_n^2}, \quad 6.$$

where k_D is a geometrical coefficient; $\overline{u_d}$ is the average velocity of the droplet; μ_c is the dynamic viscosity of the continuous phase; d is the droplet diameter; and W_n is the inner or outer diameter

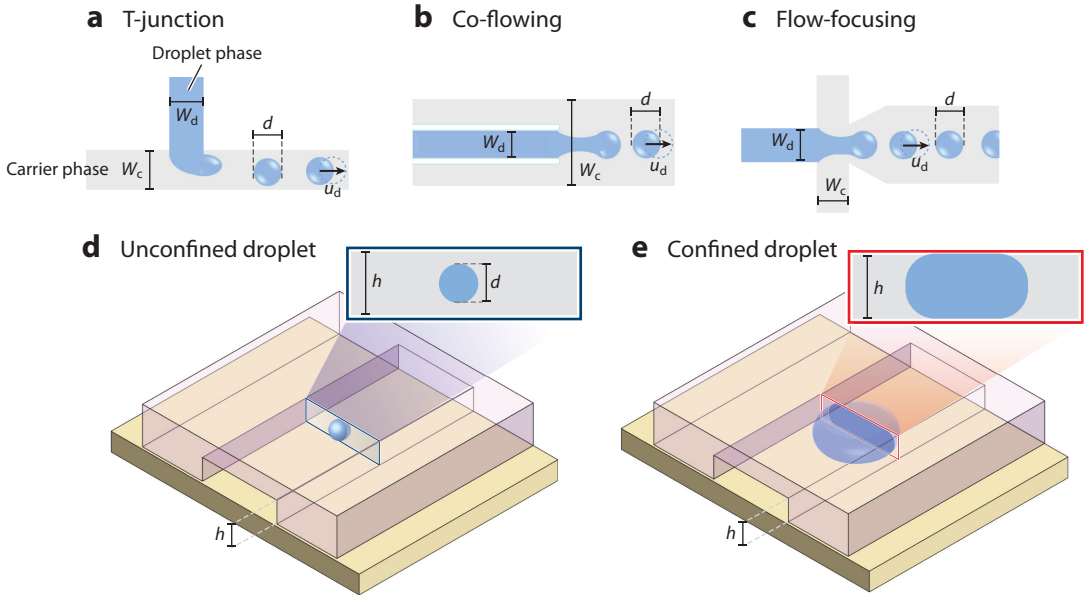

Figure 7

Illustrations of three common designs to generate droplets and bubbles: (*a*) T-junction, (*b*) co-flowing, and (*c*) flow-focusing geometry. *W* represents the width of a rectangular channel in panels *a* and *c* and the diameter of a circular channel in panel *b*. The subscripts "d" and "c" represent dispersed and continuous phase, respectively. *d* and u_d refer to the diameter and velocity, respectively, of the generated droplet or bubble. (*d*) A 3D representation of an unconfined droplet or bubble, which is spherical. (*e*) A 3D representation of a confined droplet or bubble, which is pancake shaped. In panels *d* and *e*, *h* represents the height of the channels. The insets in panels *d* and *e* show the relative dimensions and shapes of the channels and the droplet or bubble.

of the microcapillary, depending on the wetting of the channel. Both methods have the advantage of being able to be performed with high throughput, but it would be challenging to apply them to dynamic surfactant-laden interfaces with both time-dependent and curvature-dependent IFT.

2.2.5. Droplet and bubble deformation in flow using microfluidics. Microfluidic droplet deformation–based methods use changes in droplet shape induced by changes in channel geometry to determine both the dynamic and equilibrium IFT of micrometer-sized droplets. Here, a dimensionless deformation $\bar{d}$ is defined as

$$\bar{d} = \frac{d_{major} - d_{minor}}{d_{major} + d_{minor}}, \qquad 7.$$

where d_{major} and d_{minor} are defined as in **Figure 1*b***. Droplets and bubbles with diameters less than the height of the microfluidic channel are said to be unconfined (**Figure 7*d,e***), with fully unconfined droplets having diameters less than 70% of the channel height. Following the analytical solutions of the Stokes equation for the velocity and pressure fields by Lamb (93), Taylor (94, 95) derived a theoretical solution to the equilibrium deformation of unconfined droplets and bubbles assuming small deformation, no slip at the droplet interface, and continuity of tangential stress. Experimental data on droplet deformation in extensional flow using a four-mill apparatus revealed that droplet deformation increases linearly with capillary number, defined as $Ca = 2\mu_c G r_0/\sigma$ for small deformation, with $G = \frac{du}{dx}$ being the extensional rate and r_0 the radius of the undeformed

droplet (94). The linear relationship is given by

$$\bar{d} = \frac{19\mu_d + 16\mu_c}{16\mu_d + 16\mu_c} Ca \text{ (fully unconfined)}, \quad 8.$$

where μ_d and μ_c are the viscosities of the dispersed and continuous phases, respectively.

When the droplet diameter exceeds the height of the channel (**Figure 7*e*,*f***), it tends to form a pancake shape. The equilibrium deformation theory for this case has been derived from Hele-Shaw flow (96, 97), found in the fully confined limit in which the projected droplet diameter is greater than four times the channel height. The steady-state deformation of a droplet is equal to *Ca* for low values of *Ca*, i.e.,

$$\bar{d} = Ca = \frac{4\mu_c G r_0^3}{\gamma h^2} \text{ (fully confined)}. \quad 9.$$

Here r_0 represents the projected radius of the undeformed pancake-shaped droplet, which can be approximated by the geometric mean of the long and short axes of the projected ellipse shape when the droplet deforms. This fully confined deformation-based analysis has been applied to a diamond-shaped cross-slot geometry (**Figure 8*a***) in a diluted bitumen–water emulsion system (96) and in an SDS (sodium dodecyl sulfate) water–Span® 80 mineral oil system (97). Using Equation 9, the slope of the line shown in **Figure 8*c*** yields the IFT.

Besides the methods based on equilibrium deformation, an array of channel contractions and expansions placed in series has been used for measuring IFT considering dynamic deformation. Rallison (98) derived a theoretical solution for transient droplet deformation in plane hyperbolic flow for small *Ca*. A linear approximation was used because the distortion is constrained by high IFT. Later, Hudson and coworkers (99, 100) used this derivation in microfluidic channels, as shown in **Figure 8*b***, to measure IFT in droplets and bubbles. In this approach, the net deforming stress on the droplet is balanced by the interfacial or surface tension per unit length. A similar tensiometer design was used to measure the static IFT of aqueous aerosol mimics (4, 101), as shown in **Figure 8*d*** (a Taylor-Hudson plot), and secondary organic aerosols (102) in a continuous phase of oil. This approach has also been applied to unconfined droplets in both water-in-fuel (13) and oil-in-water systems (14) to find the time-dependent change in IFT due to surfactant transport to the interface. For both systems, the drop in IFT was found to occur at least an order of magnitude faster for the microscale droplets than that for the macroscale pendant drops. As with the phase measurements described in Section 2.1.4., this microfluidic approach has been extended to measure temperature-dependent IFT using on-chip heaters and sensors (103). The temperature was varied from 22°C to 70°C to study the variation in IFT with temperature for air bubbles in glycerol and glycerol–water mixtures in silicone and mineral oils. An ongoing challenge with this approach is the handling of deformations of confined droplets. Analytical solutions of the forces acting on the droplet or calibrations relating dynamic deformation to confinement are needed for accurate IFT measurement in confined droplets. Existing studies on equilibrium deformation of confined droplets (96, 97) and droplet deformation with confined channels (104, 105) could be beneficial in that regard.

2.2.6. Viscosity measurement using microfluidics: a prerequisite to microfluidic tensiometry. Microfluidic tensiometry requires prerequisite knowledge of the viscosity of the droplet phase. While bulk viscometry is a viable option in most applications, due to the submilliliter sample size in aerosol science, microfluidic measurement of viscosity is preferable. The most common type of device uses the pressure drop reading across a channel of known dimensions

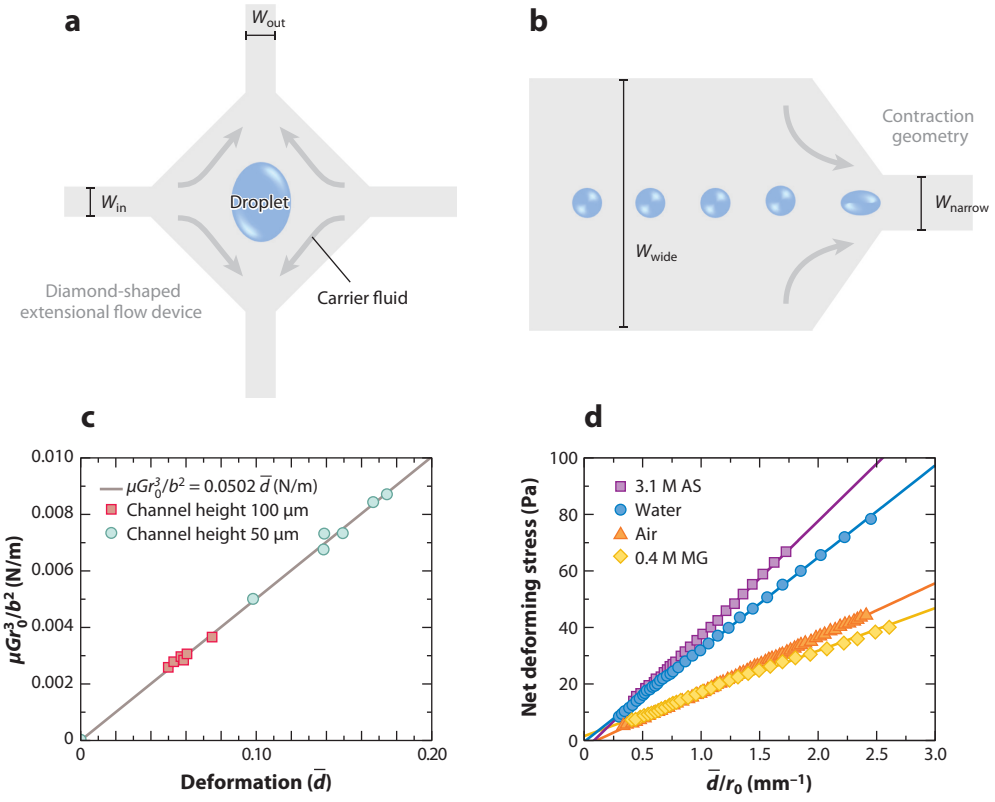

Figure 8

Droplet manipulation in microfluidic tensiometers. (*a*) Schematic of a diamond-shaped extensional flow device with a confined droplet. W represents the width of the rectangular channels and the subscripts "in" and "out" represent the width of the inlet and outlet branches, respectively. (*b*) Schematic of a contraction geometry with unconfined droplets or bubbles flowing through it. The subscripts "wide" and "narrow" refer to the wide and narrow channels, respectively. Gray arrows in panels *a* and *b* represent the flow direction of the carrier fluid. (*c*) Graph of interfacial tension (IFT) measurement based on the equilibrium deformation of confined water droplets with different heights in mineral oil. The *y* axis represents the product of nondimensional equilibrium deformation $\bar{d}$ and the IFT and the *x* axis represents $\bar{d}$. Hence the slope of the line is the IFT. The parameter b is equal to half of the channel height. Panel *c* adapted with permission from Reference 96; copyright 2019 American Chemical Society. (*d*) Graph showing the interfacial/surface tension measurement based on the dynamic deformation of unconfined droplets or bubbles with different phases, including 3.1 M ammonium sulfate (AS), water, air, and 0.4 M methylglyoxal (MG). The *y* axis represents the difference between the deforming force per unit area from extensional flow and the material change in deformation; the *x* axis represents the nondimensional deformation normalized by the droplet nominal diameter r_0. Once again, the slope of this line is the numerical value of the interfacial/surface tension. Panel *d* adapted with permission from Reference 101; copyright 2016 American Chemical Society.

with a modified form of the well-known Hagen-Poiseuille equation for a rectangular channel (1),

$$\mu = \frac{Wh\Delta P}{6QL}\left(\frac{Wh}{W+h}\right)^2, \qquad 10.$$

MEMS: microelectromechanical system

where ΔP is the pressure difference measured for flow rate Q across a rectangular channel of length L, width W, and height b. Flow rate is usually controlled in these devices by external pumps, while the pressure difference is measured using either commercially available external pressure sensors (106–108) or on-chip embedded microelectromechanical system (MEMS)-based capacitive (109, 110), piezoelectric (111, 112) or electrofluidic (113, 114) sensors. An example is shown in **Figure 9*a***.

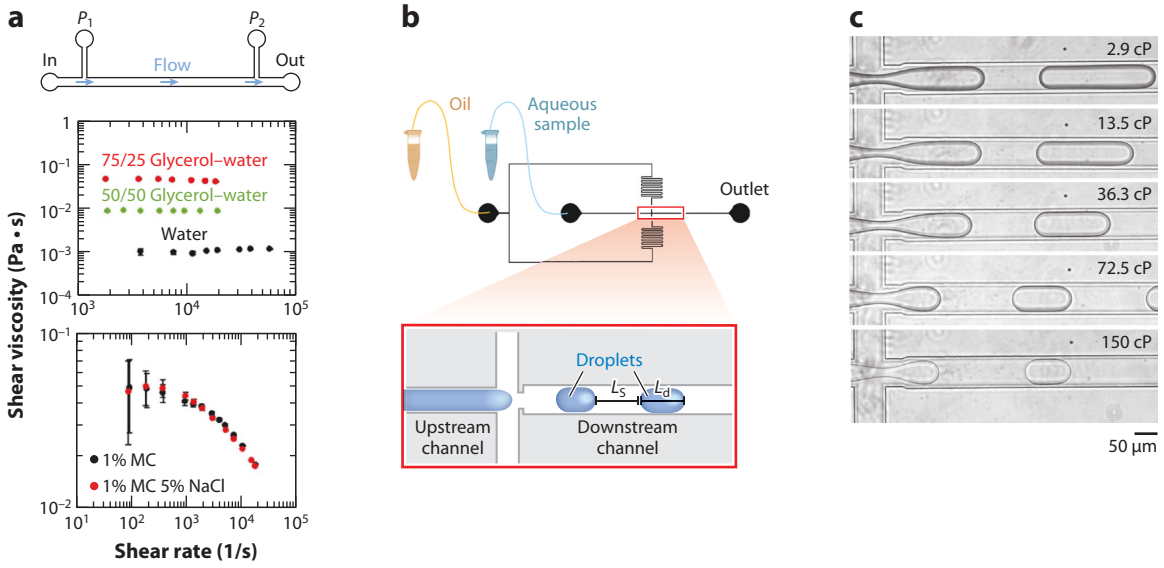

Figure 9

(*a*, *top*) Schematic of a pressure-based microfluidic viscometer for measuring the shear viscosity of continuously flowing fluids using pressure drop in a straight channel of fixed length and cross section. Here, two external pressure sensors are connected across a channel at locations P_1 and P_2. The arrows denote the flow direction. (*Bottom*) Graphs of the results showing shear viscosity as a function of shear rate for Newtonian (glycerol–water mixture) and non-Newtonian [methylcellulose (MC) and NaCl mixture] fluids. Panel *a* adapted with permission from Reference 106; copyright 2020 The Royal Society of Chemistry. (*b*) Schematic showing a droplet length–based microfluidic viscometer using two-phase flow. The space between two droplets is filled with the carrier phase fluid. L_s is the spacing between two droplets and L_d is the droplet or slug length. (*c*) Photographs showing that the length of the generated aqueous-phase droplet/slug provides a measure of its viscosity. The numbers in the photographs represent the viscosity of the droplet/slug phase. Panels *b* and *c* reproduced with permission from Reference 124; copyright 2017 American Chemical Society.

The variables measured in this type of viscometers are flow rate and pressure drop. Either external flow meters (115), flow front propagation rate inside the microchannel (116), or embedded MEMS-based flow sensors (117, 118) are used for measuring the flow rate. However, simpler devices have also been used that allow flow rates of a test fluid to be compared with a fluid of known viscosity (119, 120). In addition, capillary viscometers have been developed that allow the balance between viscous and capillary forces to be used to calculate the viscosity of a fluid with known surface tension (121).

Droplet-based techniques have also been used to measure viscosity in microfluidic devices. The relative viscosity of phases in a device controls the capillary number and hence the droplet-generation regime. Examples include measurement of droplet or fluid plug size (**Figure 9*c***) and generation frequency at different flow regimes (122, 123) as well as determination of plug velocity and spacing between plugs in multiphase flows (124). For a comprehensive review of microfluidic viscometers, refer to Gupta et al. (125).

2.3. Drop Oscillation–Based Measurements: Microscale Methods and Potential for Microfluidics

Droplet-shape oscillation dynamics (**Figure 1*c***) are governed by a droplet's physical properties, including its surface tension and viscosity. Rayleigh (126) first described the eigenfrequency of oscillation for an incompressible, inviscid, free-oscillating droplet in air by solving the governing

shape equation of an infinite series of orthogonal surface harmonics as

$$\omega_n = \frac{n(n-1)(n+2)\gamma}{\rho r_0^3}, \qquad 11.$$

where n is the oscillation mode, ρ is the density, and r_0 is the initial undisturbed radius of the droplet. Lamb (93) expanded this solution to include viscous damping internal to the droplet and derived the damping time period τ as

$$\tau = \frac{\rho r_0^2}{\mu(n-1)(2n+1)}. \qquad 12.$$

Both the surface tension and the viscosity of the droplet can be calculated when the frequency and decay time period are measured. There are several approaches and modifications to this method and corresponding governing equations in different regimes (127, 128). An excellent theoretical treatment was given by Miller & Scriven (129), who described interfacial small amplitude oscillations in multiple combinations of high and low fluid viscosities for the droplet and surrounding phases. Depending on the type of perturbation, these methods can be broadly classified into noncoalescing and coalescing.

2.3.1. Noncoalescing methods. The simplest way to trigger droplet oscillation is by gravity- or inertia-driven free motion. The droplet is ejected from an orifice with an initial velocity or is allowed to free fall. A train of droplets is imaged immediately following droplet generation. This method is usually applicable in the regime of $Bo \ll 1$ in which droplet shape is governed by capillary forces rather than by gravitational forces. Early studies showed the viability of this method with Newtonian fluids and stroboscopic light sources (130–132). Recently, high-speed cameras have enabled videos of single picoliter droplets to be captured at up to 20,000 frames per second without the need for a stroboscopic light source (133). In principle, these oscillation-based methods could be used in microfluidic channels (e.g., **Figure 1*c***) in which trapped droplets can be perturbed and oscillated in the underdamped regime used to determine IFT or viscosity. A similar approach was recently used for investigating droplet shape relaxation in the overdamped regime (134). In addition, digital microfluidics–based EWOD devices have been used to trigger droplet oscillations using alternating current in which the resonant frequency is set by a balance between droplet inertia, surface tension, friction along the contact line, and droplet internal viscous forces. These oscillations have been used to measure both the viscosity (135) and surface tension (136) of droplets (**Figure 10*a***).

2.3.2. Coalescing methods. Droplets can also be perturbed by coalescence with another droplet. These methods are more suitable for instruments in which the droplet-generation region cannot be easily observed or when there are no suitable probes to perturb the droplet when it is inside the observation zone. The simplest of the coalescing methods uses a pair of droplet generators facing each other with the droplets colliding in the field of view of a camera (137). However, this method requires very high droplet velocities (~10 mm/s) to mitigate the vertical descent due to gravity. These high shear rates result in large amplitude oscillations and cause measurement errors in high viscosity or non-Newtonian liquids.

To enable smaller oscillation amplitudes and to observe the chemical properties of the droplet prior or subsequent to coalescence as pertinent to aerosol studies, trapping methods such as holographic optical tweezers (138, 139) are used. In these methods, highly focused laser beams are used to trap and manipulate picoliter-sized droplets (**Figure 10*b***), and the oscillations can be observed using cameras or photodiodes. Miles et al. (140) recently used a combination of the coalescing

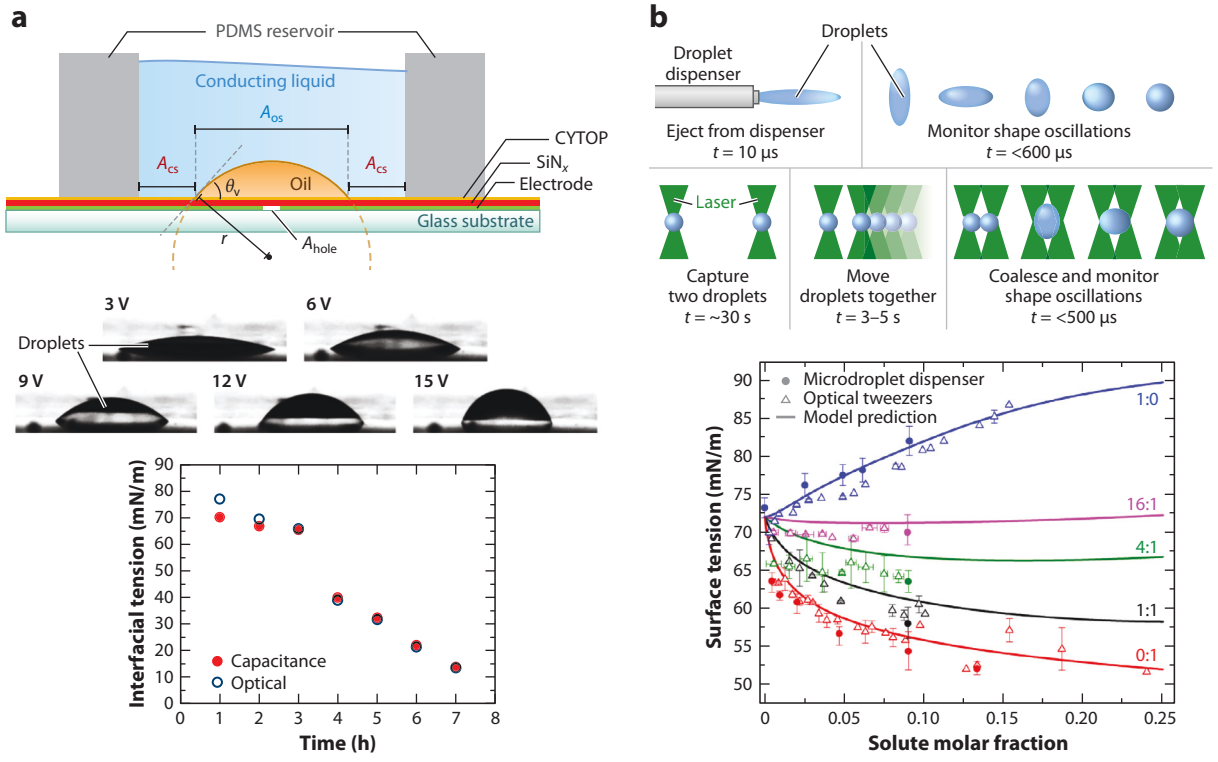

Figure 10

(*a*) Schematic illustration of a digital microfluidics–based droplet oscillation tensiometer and representative results. (*Top*) The electrode is capped with a dielectric layer of silicon nitride (SiN_x) and hydrophobic layer of CYTOP™, which is a commercial fluoropolymer coating. *A* refers to area and the subscripts "os," "cs," and "hole" refer to droplet wetted, conducting liquid wetted, and electrode hole, respectively. The electrode hole pins the droplet at the center of the electrode during electrowetting. θ_V is the contact angle of the droplet; *r* is the radius of the curved droplet/conducting liquid interface. (*Middle*) The droplet area and contact angle change with applied voltage, shown in the top left of each droplet photograph. (*Bottom*) Graph showing how the IFT of an n-decane droplet laden with the surfactant Tween® 80 immersed in an Na_2SO_4 solution changes with time. The droplet shape was estimated both optically and using the electrode capacitance. This change in shape was used to calculate the IFT of a sessile oil droplet in water. Panel *a* adapted with permission from Reference 136; copyright 2014 AIP Publishing. (*b*, *top*) Illustrations of droplet oscillations created with both noncoalescing and coalescing methods in an optical tweezer. (*Bottom*) Graph of surface tension values compared for both methods as a function of solute concentration in the droplet. Mass ratios of different systems of NaCl and glutaric acid are indicated next to the curves. Closed symbols represent droplet dispenser readings, open symbols represent optical tweezer readings, and solid lines represent model predictions. Panel *b* adapted with permission from Reference 140; copyright 2019 American Chemical Society. Abbreviations: IFT, interfacial tension; PDMS, poly(dimethylsiloxane).

and noncoalescing oscillation methods and showed that these methods are equivalent for aerosol systems (**Figure 10*b***). In addition, an electrodynamic balance has been adapted for the simultaneous trapping of two droplets for coalescence (141). Microfluidic devices that incorporate optical tweezers to trap solid particles immersed in test fluid have been developed (142, 143); however, these methods use the motion of the particles inside the fluid to measure viscosity rather than the oscillation of the fluid itself. Additionally, coalescence-based methods have also been used for observing the surface rheological properties of surfactant-laden systems at both micro and macro scales (144, 145).

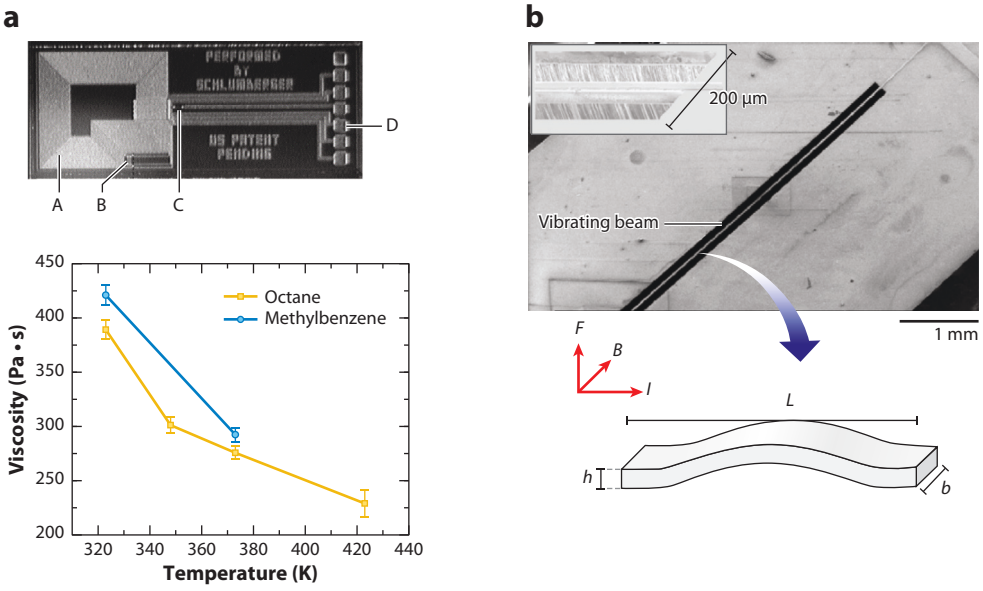

Figure 11

(*a*, *top*) Photograph of a microelectromechanical system (MEMS) cantilever for measuring viscosity using change in resonant frequency when immersed in different samples. The aluminum coil (A), Wheatstone bridge (B), resistive thermometer (C), and wire bond pads (D) for the cantilever are indicated by lines. Panel *a* top adapted with permission from Reference 147; copyright 2006 American Chemical Society. (*Bottom*) Graph showing measured viscosities of two different samples at different temperatures using the device. Panel *a* bottom, data from Reference 147. (*b*, *top*) Scanning electron micrograph showing a plan view of a silicon on insulator MEMS cantilever for measuring the viscosity of flowing fluid. The bright areas show the silicon and the dark regions show voids for the flow channels. The thin bright line inside the two dark regions in the center is the actual double-clamped cantilever beam. The inset shows a low-angle magnified view of the beam suspended in a 200-µm-wide channel. The different layers are the layers of the silicon on the insulator wafer. (*Bottom*) Illustrations showing beam dimensions and deflected shape for the double-clamped beam; the beam has a length (*L*) of 1.5, 2, 3, or 5 mm, a width (*b*) of 30 or 50 µm, and a thickness (*h*) of 20 µm. The red axes show the directions of the current flow (*I*), magnetic field (*B*), and the resulting Lorentz force (*F*), which deflects the beam along the fluid flow direction. Panel *b* adapted with permission from Reference 148; copyright 2007 Elsevier Science.

2.4. Deflection-Based Methods: Microscale Methods and the Potential for Microfluidics

Methods in which deflection and vibration of an external probe provide a measure of viscosity and surface tension (**Figure 1*d***) could also be applied to microfluidic devices. An excellent example of this is provided by MEMS devices, which are fabricated with microfabrication techniques and used as sensors and actuators in micro- to nanoscale systems (146) such as inkjet printing and telecommunication and biomedical devices. The resonant frequencies of immersed cantilever-type MEMS devices are used to measure the viscosity of the surrounding fluid with a cantilever strain gauge (147, 148) (**Figure 11*a***) or a suspended oscillating plate (149) configuration. A novel cantilever array configuration with measurement of static deflection has also been used to measure the surface tension of water in a limited capacity (150). MEMS-based sensors have also been integrated into microfluidic devices (**Figure 11*b***) for continuous monitoring of fluid viscosity in a flow channel (148). Quartz crystal microbalances (QCMs) are a similar class of devices that measure changes in the resonating frequency of a quartz crystal due to changes in mass and are commonly

QCM: quartz crystal microbalance

used in the semiconductor industry to monitor thin-film deposition at rates as small as 1 ng/cm^2. QCMs have been used to monitor water uptake and phase change of dry deposited aerosols under changing RH conditions (151, 152). Finally, force microscopy methods including atomic force microscopy, the poke-flow technique, and other indentation-based methods have also been used to study the phase state and surface tension of aerosol particles and thin films at nanometer to micrometer length scales. For details about these methods, see the reviews by Lee & Tivanski (9) and Reid et al. (5).

3. CONCLUSIONS

Aerosols, emulsions, suspensions, and biological fluids are complex multiphase systems with dynamic properties often dependent on the length scale of the dispersed phase. Microscale techniques for quantitative physical and chemical characterization are required to measure time- or curvature-dependent properties. We have reviewed a number of important microscale methods for measuring properties such as viscosity, IFT, and phase transitions of the dispersed phase droplet, including both static and microfluidic approaches. In particular, microfluidic approaches offer the advantages of high throughput with small sample volumes and tunable droplet sizes. As the field of microfluidics advances, existing microfluidic phase measurements are being further augmented with chemical characterization techniques such as Raman spectroscopy, Fourier transform infrared spectroscopy, and mass spectroscopy as well as advanced measurements using on-chip temperature or pressure sensors or multilayered designs. We can expect these techniques to become more affordable, robust, and able to harvest a wider range of data from smaller samples with easier operation as microfabrication techniques and imaging technologies improve, leading to tremendous improvements in field deployment for remote data collection and fundamental research in applications ranging from aerosol science to liquid separation.

DISCLOSURE STATEMENT

The authors are not aware of any affiliations, memberships, funding, or financial holdings that might be perceived as affecting the objectivity of this review. Any opinions, findings, and conclusions or recommendations expressed in this material are those of the authors and do not necessarily reflect the views of the National Science Foundation.

ACKNOWLEDGMENTS

This work was supported in part by the National Science Foundation (NSF) through the NSF Center for Aerosol Impacts on Chemistry of the Environment (CAICE), an NSF Funded Center for Chemical Innovation (grant CHE-1801971), which was the primary source of support for graduate student P.R. This work was also supported in part by the NSF under NSF CAREER Grant No. 1554936, which was the primary source of support for graduate student S.L.

LITERATURE CITED

1. Pipe CJ, McKinley GH. 2009. Microfluidic rheometry. *Mech. Res. Commun.* 36(1):110–20
2. Mukhopadhyay A, Granick S. 2001. Micro- and nanorheology. *Curr. Opin. Colloid Interface Sci.* 6(5–6):423–29
3. Seinfeld JH, Pandis SN. 2016. *Atmospheric Chemistry and Physics: From Air Pollution to Climate Change*. Hoboken, NJ: John Wiley & Sons. 3rd ed.

4. Boyer HC, Dutcher CS. 2017. Atmospheric aqueous aerosol surface tensions: isotherm-based modeling and biphasic microfluidic measurements. *J. Phys. Chem. A* 121(25):4733–42
5. Reid JP, Bertram AK, Topping DO, Laskin A, Martin ST, et al. 2018. The viscosity of atmospherically relevant organic particles. *Nat. Commun.* 9:956
6. Freedman MA. 2017. Phase separation in organic aerosol. *Chem. Soc. Rev.* 46(24):7694–705
7. Kanji ZA, Ladino LA, Wex H, Boose Y, Burkert-Kohn M, et al. 2017. Overview of ice nucleating particles. *Meteorol. Monogr.* 58:1.1–33
8. Sullivan RC, Gorkowski K, Jahn L. 2018. Characterization of individual aerosol particles. In *Physical Chemistry of Gas-Liquid Interfaces*, ed. JA Faust, JE House, pp. 353–402. Amsterdam: Elsevier
9. Lee HD, Tivanski AV. 2021. Atomic force microscopy: an emerging tool in measuring the phase state and surface tension of individual aerosol particles. *Annu. Rev. Phys. Chem.* 72:235–52
10. Sackmann EK, Fulton AL, Beebe DJ. 2014. The present and future role of microfluidics in biomedical research. *Nature* 507(7491):181–89
11. Lifton VA. 2016. Microfluidics: an enabling screening technology for enhanced oil recovery (EOR). *Lab Chip* 16(10):1777–96
12. Jokerst JC, Emory JM, Henry CS. 2012. Advances in microfluidics for environmental analysis. *Analyst* 137:24–34
13. Narayan S, Moravec DB, Hauser BG, Dallas AJ, Dutcher CS. 2018. Removing water from diesel fuel: understanding the impact of droplet size on dynamic interfacial tension of water-in-fuel emulsions. *Energy Fuels* 32:7326–37
14. Chen Y, Dutcher CS. 2020. Size dependent droplet interfacial tension and surfactant transport in liquid–liquid systems, with applications in shipboard oily bilgewater emulsions. *Soft Matter* 16(12):2994–3004
15. Metcalf AR, Narayan S, Dutcher CS. 2018. A review of microfluidic concepts and applications for atmospheric aerosol science. *Aerosol Sci. Technol.* 52(3):310–29
16. You Y, Smith ML, Song M, Martin ST, Bertram AK. 2014. Liquid–liquid phase separation in atmospherically relevant particles consisting of organic species and inorganic salts. *Int. Rev. Phys. Chem.* 33(1):43–77
17. Losey DJ, Parker RG, Freedman MA. 2016. pH dependence of liquid–liquid phase separation in organic aerosol. *J. Phys. Chem. Lett.* 7(19):3861–65
18. Song M, Marcolli C, Krieger UK, Zuend A, Peter T. 2012. Liquid-liquid phase separation and morphology of internally mixed dicarboxylic acids/ammonium sulfate/water particles. *Atmos. Chem. Phys.* 12(5):2691–712
19. Tong H-J, Qian Z-G, Reid JP, Zhang Y-H. 2011. High temporal and spatial resolution measurements of the rapid efflorescence of sea salt droplets. *Acta Phys. Chim. Sin.* 27(11):2521–27
20. Wise ME, Baustian KJ, Koop T, Freedman MA, Jensen EJ, Tolbert MA. 2012. Depositional ice nucleation onto crystalline hydrated NaCl particles: a new mechanism for ice formation in the troposphere. *Atmos. Chem. Phys.* 12(2):1121–34
21. Wise ME, Baustian KJ, Tolbert MA. 2010. Internally mixed sulfate and organic particles as potential ice nuclei in the tropical tropopause region. *PNAS* 107(15):6693–98
22. Baustian KJ, Cziczo DJ, Wise ME, Pratt KA, Kulkarni G, et al. 2012. Importance of aerosol composition, mixing state, and morphology for heterogeneous ice nucleation: a combined field and laboratory approach. *J. Geophys. Res. Atmos.* 117(D6). **https://doi.org/10.1029/2011JD016784**
23. Schill GP, Tolbert MA. 2013. Heterogeneous ice nucleation on phase-separated organic-sulfate particles: effect of liquid versus glassy coatings. *Atmos. Chem. Phys.* 13(9):4681–95
24. Mael LE, Busse H, Grassian VH. 2019. Measurements of immersion freezing and heterogeneous chemistry of atmospherically relevant single particles with micro-Raman spectroscopy. *Anal. Chem.* 91(17):11138–45
25. You Y, Renbaum-Wolff L, Carreras-Sospedra M, Hanna SJ, Hiranuma N, et al. 2012. Images reveal that atmospheric particles can undergo liquid–liquid phase separations. *PNAS* 109(33):13188–93
26. Hosny NA, Fitzgerald C, Vyšniauskas A, Athanasiadis A, Berkemeier T, et al. 2016. Direct imaging of changes in aerosol particle viscosity upon hydration and chemical aging. *Chem. Sci.* 7(2):1357–67
27. Waigh TA. 2005. Microrheology of complex fluids. *Rep. Prog. Phys.* 68(3):685–742
28. Dutcher CS, Woehl TJ, Talken NH, Ristenpart WD. 2013. Hexatic-to-disorder transition in colloidal crystals near electrodes: rapid annealing of polycrystalline domains. *Phys. Rev. Lett.* 111(12):128302

29. Tokarev A, Aprelev A, Zakharov MN, Korneva G, Gogotsi Y, Kornev KG. 2012. Multifunctional magnetic rotator for micro and nanorheological studies. *Rev. Sci. Instrum.* 83(6):065110
30. Renbaum-Wolff L, Grayson JW, Bertram AK. 2013. Technical note: new methodology for measuring viscosities in small volumes characteristic of environmental chamber particle samples. *Atmos. Chem. Phys.* 13(2):791–802
31. Ren K, Zhou J, Wu H. 2013. Materials for microfluidic chip fabrication. *Acc. Chem. Res.* 46(11):2396–406
32. McDonald JC, Duffy DC, Anderson JR, Chiu DT, Wu H, et al. 2000. Fabrication of microfluidic systems in poly(dimethylsiloxane). *Electrophoresis* 21(1):27–40
33. Randall GC, Doyle PS. 2005. Permeation-driven flow in poly(dimethylsiloxane) microfluidic devices. *PNAS* 102(31):10813–18
34. Nandy L, Liu S, Gunsbury C, Wang X, Pendergraft MA, et al. 2019. Multistep phase transitions in sea surface microlayer droplets and aerosol mimics using microfluidic wells. *ACS Earth Space Chem.* 3(7):1260–67
35. Roy P, Mael LE, Makhnenko I, Martz R, Grassian VH, Dutcher CS. 2020. Temperature-dependent phase transitions of aqueous aerosol droplet systems in microfluidic traps. *ACS Earth Space Chem.* 4(9):1527–39
36. Bithi SS, Vanapalli SA. 2010. Behavior of a train of droplets in a fluidic network with hydrodynamic traps. *Biomicrofluidics* 4(4):044110
37. Boukellal H, Selimović E, Jia Y, Cristobal G, Fraden S. 2009. Simple, robust storage of drops and fluids in a microfluidic device. *Lab Chip* 9(2):331–38
38. Selimović E, Gobeaux F, Fraden S. 2010. Mapping and manipulating temperature–concentration phase diagrams using microfluidics. *Lab Chip* 10(13):1696–99
39. Wang W, Yang C, Li CM. 2009. On-demand microfluidic droplet trapping and fusion for on-chip static droplet assays. *Lab Chip* 9(11):1504–6
40. Nandy L, Dutcher CS. 2018. Phase behavior of ammonium sulfate with organic acid solutions in aqueous aerosol mimics using microfluidic traps. *J. Phys. Chem. B* 122(13):3480–90
41. Bleier BJ, Anna SL, Walker LM. 2018. Microfluidic droplet-based tool to determine phase behavior of a fluid system with high composition resolution. *J. Phys. Chem. B* 122(14):4067–76
42. Boreyko JB, Mruetusatorn P, Retterer ST, Collier CP. 2013. Aqueous two-phase microdroplets with reversible phase transitions. *Lab Chip* 13(7):1295–301
43. Jung SY, Retterer ST, Collier CP. 2010. On-demand generation of monodisperse femtolitre droplets by shape-induced shear. *Lab Chip* 10(20):2688–94
44. Shim JU, Cristobal G, Link DR, Thorsen T, Jia Y, et al. 2007. Control and measurement of the phase behavior of aqueous solutions using microfluidics. *J. Am. Chem. Soc.* 129(28):8825–35
45. Cohen DE, Schneider T, Wang M, Chiu DT. 2010. Self-digitization of sample volumes. *Anal. Chem.* 82(13):5707–17
46. Polen M, Lawlis E, Sullivan RC. 2016. The unstable ice nucleation properties of Snomax® bacterial particles. *J. Geophys. Res. Atmos.* 121:11666–78
47. Polen M, Brubaker T, Somers J, Sullivan RC. 2018. Cleaning up our water: reducing interferences from nonhomogeneous freezing of "pure" water in droplet freezing assays of ice-nucleating particles. *Atmos. Meas. Tech.* 11(9):5315–34
48. Leng J, Lonetti B, Tabeling P, Joanicot M, Ajdari A. 2006. Microevaporators for kinetic exploration of phase diagrams. *Phys. Rev. Lett.* 96(8):084503
49. Moreau P, Dehmoune J, Salmon JB, Leng J. 2009. Microevaporators with accumulators for the screening of phase diagrams of aqueous solutions. *Appl. Phys. Lett.* 95(3):033108
50. Chao Y, Mak SY, Rahman S, Zhu S, Shum HC. 2018. Generation of high-order all-aqueous emulsion drops by osmosis-driven phase separation. *Small* 14(39):1802107
51. Laval P, Crombez A, Salmon JB. 2009. Microfluidic droplet method for nucleation kinetics measurements. *Langmuir* 25(3):1836–41
52. Sugiyama M, Gasperino D, Derby JJ, Barocas VH. 2008. Protein–salt–water solution phase diagram determination by a combined experimental–computational scheme. *Cryst. Growth Des.* 8(12):4208–14
53. Wang H, Khodaparast S, Carroll J, Kelly C, Robles ESJ, Cabral JT. 2020. A microfluidic-multiwell platform for rapid phase mapping of surfactant solutions. *Rev. Sci. Instrum.* 91(4):45109

54. Hübner M, Minceva M. 2020. Microfluidics approach for determination of the miscibility gap of multicomponent liquid-liquid systems. *Exp. Therm. Fluid Sci.* 112:109971
55. Silva DFC, Azevedo AM, Fernandes P, Chu V, Conde JP, Aires-Barros MR. 2014. Determination of aqueous two phase system binodal curves using a microfluidic device. *J. Chromatogr. A* 1370:115–20
56. Bao B, Riordon J, Xu Y, Li H, Sinton D. 2016. Direct measurement of the fluid phase diagram. *Anal. Chem.* 88:2
57. Xu Y, Riordon J, Cheng X, Bao B, Sinton D. 2017. The full pressure-temperature phase envelope of a mixture in 1000 microfluidic chambers. *Angew. Chem. Int. Ed.* 56(45):13962–67
58. Toprakcioglu Z, Challa PK, Levin A, Knowles TPJ. 2018. Observation of molecular self-assembly events in massively parallel microdroplet arrays. *Lab Chip* 18(21):3303–9
59. Brubaker T, Polen M, Cheng P, Ekambaram V, Somers J, et al. 2019. Development and characterization of a "store and create" microfluidic device to determine the heterogeneous freezing properties of ice nucleating particles. *Aerosol Sci. Technol.* 54(1):79–93
60. Lau BTC, Baitz CA, Dong XP, Hansen CL. 2007. A complete microfluidic screening platform for rational protein crystallization. *J. Am. Chem. Soc.* 129(3):454–55
61. Zhang Y, Nguyen N-T. 2017. Magnetic digital microfluidics—a review. *Lab Chip* 17(6):994–1008
62. Choi K, Ng AHC, Fobel R, Wheeler AR. 2012. Digital microfluidics. *Annu. Rev. Anal. Chem.* 5:413–40
63. Lin Y-Y, Lin C-W, Yang L-J, Wang A-B. 2007. Micro-viscometer based on electrowetting on dielectric. *Electrochim. Acta* 52(8):2876–83
64. Tröls A, Clara S, Jakoby B. 2016. A low-cost viscosity sensor based on electrowetting on dielectrics (EWOD) forces. *Sens. Actuators A Phys.* 244:261–69
65. De Ruiter R, Wennink P, Banpurkar AG, Duits MHG, Mugele F. 2012. Use of electrowetting to measure dynamic interfacial tensions of a microdrop. *Lab Chip* 12(16):2832–36
66. Davoust L, Theisen J. 2013. Evaporation rate of drop arrays within a digital microfluidic system. *Sens. Actuators B Chem.* 189:157–64
67. Brassard D, Malic L, Normandin F, Tabrizian M, Veres T. 2008. Water-oil core-shell droplets for electrowetting-based digital microfluidic devices. *Lab Chip* 8(8):1342–49
68. DeMott PJ, Prenni AJ, Liu X, Kreidenweis SM, Petters MD, et al. 2010. Predicting global atmospheric ice nuclei distributions and their impacts on climate. *PNAS* 107(25):11217–22
69. Murray BJ, O'Sullivan D, Atkinson JD, Webb ME. 2012. Ice nucleation by particles immersed in supercooled cloud droplets. *Chem. Soc. Rev.* 41(19):6519–54
70. Hill TCJ, Moffett BF, DeMott PJ, Georgakopoulos DG, Stump WL, Franc GD. 2014. Measurement of ice nucleation-active bacteria on plants and in precipitation by quantitative PCR. *Appl. Environ. Microbiol.* 80(4):1256–67
71. Murray BJ, Broadley SL, Wilson TW, Bull SJ, Wills RH, et al. 2010. Kinetics of the homogeneous freezing of water. *Phys. Chem. Chem. Phys.* 12(35):10380–87
72. Whale TF, Murray BJ, O'Sullivan D, Wilson TW, Umo NS, et al. 2015. A technique for quantifying heterogeneous ice nucleation in microlitre supercooled water droplets. *Atmos. Meas. Tech.* 8(6):2437–47
73. Riechers B, Wittbracht F, Hütten A, Koop T. 2013. The homogeneous ice nucleation rate of water droplets produced in a microfluidic device and the role of temperature uncertainty. *Phys. Chem. Chem. Phys.* 15(16):5873–87
74. Tarn MD, Sikora SNF, Porter GCE, O'Sullivan D, Adams M, et al. 2018. The study of atmospheric ice-nucleating particles via microfluidically generated droplets. *Microfluid. Nanofluidics* 22:52
75. Stan CA, Schneider GF, Shevkoplyas SS, Hashimoto M, Ibanescu M, et al. 2009. A microfluidic apparatus for the study of ice nucleation in supercooled water drops. *Lab Chip* 9(16):2293–305
76. Young T. 1805. III. An essay on the cohesion of fluids. *Philos. Trans. R. Soc.* 95:65–87
77. Rehbinder P. 1924. Über die Abhängigkeit der Oberflächenaktivität und der Oberflächenspannung der Lösungen von der Temperatur und Konzentration. I. *Z. Phys. Chem.* 111U(1):447–64
78. Bendure RL. 1971. Dynamic surface tension determination with the maximum bubble pressure method. *J. Colloid Interface Sci.* 35(2):238–48
79. Alvarez NJ, Walker LM, Anna SL. 2010. A microtensiometer to probe the effect of radius of curvature on surfactant transport to a spherical interface. *Langmuir* 26(16):13310–19

80. Lee S, Kim DH, Needham D. 2001. Equilibrium and dynamic interfacial tension measurements at microscopic interfaces using a micropipet technique. 1. A new method for determination of interfacial tension. *Langmuir* 17(18):5537–43
81. Gu H, Duits MHG, Mugele F. 2011. Interfacial tension measurements with microfluidic tapered channels. *Colloids Surfaces A Physicochem. Eng. Asp.* 389(1–3):38–42
82. Zhou H, Yao Y, Chen Q, Li G, Yao S. 2013. A facile microfluidic strategy for measuring interfacial tension. *Appl. Phys. Lett.* 103(23):234102
83. Li S, Xu J, Wang Y, Luo G. 2009. A new interfacial tension measurement method through a pore array micro-structured device. *J. Colloid Interface Sci.* 331(1):127–31
84. Honaker LW, Lagerwall JPF, Jampani VSR. 2018. Microfluidic tensiometry technique for the characterization of the interfacial tension between immiscible liquids. *Langmuir* 34(7):2403–9
85. Lan W, Wang Z, Wang M, Liu D, Guo X, et al. 2019. Determination of transient interfacial tension in a microfluidic device using a Laplace sensor. *Chem. Eng. Sci.* 209:115207
86. Vonnegut B. 1942. Rotating bubble method for the determination of surface and interfacial tensions. *Rev. Sci. Instrum.* 13(1):6–9
87. Drelich J, Fang CH, White CL. 2002. Measurement of interfacial tension in fluid-fluid systems. In *Encyclopedia of Surface and Colloid Science*, Vol. 3, ed. AT Hubbard, P Somasundaran, pp. 3152–66. New York, NY: Marcel Dekker
88. KRÜSS Sci. 2020. *Drop shape analyzer needle specifications*. Broch., KRÜSS Sci., Hamburg, Ger. **https://www.kruss-scientific.com/fileadmin/user_upload/website/brochures/kruss-bro-acc-dsa-needle-specifications-en.pdf**
89. Zhu P, Wang L. 2017. Passive and active droplet generation with microfluidics: a review. *Lab Chip* 17(1):34–75
90. Anna SL. 2016. Droplets and bubbles in microfluidic devices. *Annu. Rev. Fluid Mech.* 48:285–309
91. Nguyen N-T, Lassemono S, Chollet FA, Yang C. 2006. Microfluidic sensor for dynamic surface tension measurement. *IEEE Proc. Nanobiotechnol.* 153(4):102–6
92. Xu JH, Li SW, Lan WJ, Luo GS. 2008. Microfluidic approach for rapid interfacial tension measurement. *Langmuir* 24(19):11287–92
93. Lamb H. 2015 (1932). *Hydrodynamics*. New York, NY: Dover. 6th ed.
94. Taylor GI. 1934. The formation of emulsions in definable fields of flow. *Proc. R. Soc. A Math. Phys. Eng. Sci.* 146(858):501–23
95. Taylor GI. 1932. The viscosity of a fluid containing small drops of another fluid. *Proc. R. Soc. A Math. Phys. Eng. Sci.* 138(834):41–48
96. Goel S, Joshi N, Uddin MS, Ng S, Acosta E, Ramachandran A. 2019. Interfacial tension of the water-diluted bitumen interface at high bitumen concentrations measured using a microfluidic technique. *Langmuir* 35(48):15710–22
97. Motagamwala AH. 2013. *A microfluidic, extensional flow device for manipulating soft particles*. MS Thesis, Univ. Toronto
98. Rallison J. 1984. The deformation of small viscous drops and bubbles in shear flows. *Annu. Rev. Fluid Mech.* 16:45–66
99. Hudson SD, Cabral JT, Goodrum WJ, Beers KL, Amis EJ. 2005. Microfluidic interfacial tensiometry. *Appl. Phys. Lett.* 87(8):081905
100. Cabral JT, Hudson SD. 2006. Microfluidic approach for rapid multicomponent interfacial tensiometry. *Lab Chip* 6(3):427–36
101. Metcalf AR, Boyer HC, Dutcher CS. 2016. Interfacial tensions of aged organic aerosol particle mimics using a biphasic microfluidic platform. *Environ. Sci. Technol.* 50(3):1251–59
102. Riva M, Chen Y, Zhang Y, Lei Z, Olson NE, et al. 2019. Increasing isoprene epoxydiol-to-inorganic sulfate aerosol ratio results in extensive conversion of inorganic sulfate to organosulfur forms: implications for aerosol physicochemical properties. *Environ. Sci. Technol.* 53(15):8682–94
103. Lee D, Fang C, Ravan AS, Fuller GG, Shen AQ. 2017. Temperature controlled tensiometry using droplet microfluidics. *Lab Chip* 17(4):717–26
104. Brosseau Q. 2014. *Dynamics of soft interfaces in droplet-based microfluidics*. PhD Thesis, Georg-August Univ., Göttingen, Ger.

105. Brosseau Q, Vrignon J, Baret JC. 2014. Microfluidic dynamic interfacial tensiometry (μDIT). *Soft Matter* 10(17):3066–76
106. Micklavzina B, Metaxas A, Dutcher CS. 2020. Microfluidic rheology of methylcellulose solutions in hyperbolic contractions and the effect of salt in shear and extensional flows. *Soft Matter* 16:5273–81
107. Kang K, Lee LJ, Koelling KW. 2005. High shear microfluidics and its application in rheological measurement. *Exp. Fluids* 38(2):222–32
108. Wang J, James DF. 2011. Lubricated extensional flow of viscoelastic fluids in a convergent microchannel. *J. Rheol.* 55(5):1103–26
109. Pipe CJ, Majmudar TS, McKinley GH. 2008. High shear rate viscometry. *Rheol. Acta* 47(5–6):621–42
110. Ober TJ, Haward SJ, Pipe CJ, Soulages J, McKinley GH. 2013. Microfluidic extensional rheometry using a hyperbolic contraction geometry. *Rheol. Acta* 52(6):529–46
111. Quist A, Chand A, Ramachandran S, Cohen D, Lal R. 2006. Piezoresistive cantilever based nanoflow and viscosity sensor for microchannels. *Lab Chip* 6(11):1450–54
112. Kim HJ, Kim J, Zandieh O, Chae MS, Kim TS, et al. 2014. Piezoelectric layer embedded-microdiaphragm sensors for the determination of blood viscosity and density. *Appl. Phys. Lett.* 105(15):153504
113. Liu MC, Shih HC, Wu JG, Weng TW, Wu CY, et al. 2013. Electrofluidic pressure sensor embedded microfluidic device: a study of endothelial cells under hydrostatic pressure and shear stress combinations. *Lab Chip* 13(9):1743–53
114. Lee T-A, Liao W-H, Tung Y-C. 2017. Fully disposable and optically transparent microfluidic viscometer based on electrofluidic pressure sensor. In *2017 19th International Conference on Solid-State Sensors, Actuators, and Microsystems (TRANSDUCERS 2017)*, pp. 579–82. Piscataway, NJ: IEEE
115. Hudson SD, Sarangapani P, Pathak JA, Migler KB. 2015. A microliter capillary rheometer for characterization of protein solutions. *J. Pharm. Sci.* 104(2):678–85
116. Solomon DE, Abdel-Raziq A, Vanapalli SA. 2016. A stress-controlled microfluidic shear viscometer based on smartphone imaging. *Rheol. Acta* 55(9):727–38
117. Zarifi MH, Sadabadi H, Hejazi SH, Daneshmand M, Sanati-Nezhad A. 2018. Noncontact and nonintrusive microwave-microfluidic flow sensor for energy and biomedical engineering. *Sci. Rep.* 8(1):139
118. Noeth N, Keller SS, Boisen A. 2013. Integrated cantilever-based flow sensors with tunable sensitivity for in-line monitoring of flow fluctuations in microfluidic systems. *Sensors* 14(1):229–44
119. Lee J, Tripathi A. 2005. Intrinsic viscosity of polymers and biopolymers measured by microchip. *Anal. Chem.* 77(22):7137–47
120. Solomon DE, Vanapalli SA. 2014. Multiplexed microfluidic viscometer for high-throughput complex fluid rheology. *Microfluid. Nanofluidics* 16(4):677–90
121. Srivastava N, Davenport RD, Burns MA. 2005. Nanoliter viscometer for analyzing blood plasma and other liquid samples. *Anal. Chem.* 77(2):383–92
122. Delamarre MF, Keyzer A, Shippy SA. 2015. Development of a simple droplet-based microfluidic capillary viscometer for low-viscosity Newtonian fluids. *Anal. Chem.* 87(9):4649–57
123. Nie Z, Seo MS, Xu S, Lewis PC, Mok M, et al. 2008. Emulsification in a microfluidic flow-focusing device: effect of the viscosities of the liquids. *Microfluid. Nanofluidics* 5(5):585–94
124. Li Y, Ward KR, Burns MA. 2017. Viscosity measurements using microfluidic droplet length. *Anal. Chem.* 89(7):3996–4006
125. Gupta S, Wang WS, Vanapalli SA. 2016. Microfluidic viscometers for shear rheology of complex fluids and biofluids. *Biomicrofluidics* 10:43402
126. Strutt JW (Lord Rayleigh). 1879. VI. On the capillary phenomena of jets. *Proc. R. Soc.* 29(196–199):71–97
127. Prosperetti A. 1980. Free oscillations of drops and bubbles: the initial-value problem. *J. Fluid Mech.* 100(2):333–47
128. Suryanarayana PVR, Bayazitoglu Y. 1991. Surface tension and viscosity from damped free oscillations of viscous droplets. *Int. J. Thermophys.* 12(1):137–51
129. Miller CA, Scriven LE. 1968. The oscillations of a fluid droplet immersed in another fluid. *J. Fluid Mech.* 32(3):417–35

130. Hiller WJ, Kowalewski TA. 1989. Optical investigation of oscillating liquid droplets. *Z. Angew. Math. Mech.* 69(6):T629–78
131. Trinh E, Zwern A, Wang TG. 1982. An experimental study of small-amplitude drop oscillations in immiscible liquid systems. *J. Fluid Mech.* 115:453–74
132. Brenn G, Frohn A. 1993. An experimental method for the investigation of droplet oscillations in a gaseous medium. *Exp. Fluids* 15(2):85–90
133. Staat HJJ, van der Bos A, van den Berg M, Reinten H, Wijshoff H, et al. 2017. Ultrafast imaging method to measure surface tension and viscosity of inkjet-printed droplets in flight. *Exp. Fluids* 58:2
134. Narayan S, Moravec DB, Dallas AJ, Dutcher CS. 2020. Droplet shape relaxation in a four-channel microfluidic hydrodynamic trap. *Phys. Rev. Fluids* 5:113603
135. Hong J, Kim YK, Kang KH, Kim J, Lee SJ. 2014. Effects of drop viscosity on oscillation dynamics induced by AC electrowetting. *Sens. Actuators B Chem.* 190:48–54
136. Choi S, Kwon Y, Lee J. 2014. Electrowetting-based measurement of interfacial tension. *Appl. Phys. Lett.* 105:183509
137. Yamada T, Sakai K. 2012. Observation of collision and oscillation of microdroplets with extremely large shear deformation. *Phys. Fluids* 24(2):022103
138. Bzdek BR, Power RM, Simpson SH, Reid JP, Royall CP. 2016. Precise, contactless measurements of the surface tension of picolitre aerosol droplets. *Chem. Sci.* 7(1):274–85
139. Power RM, Reid JP. 2014. Probing the micro-rheological properties of aerosol particles using optical tweezers. *Rep. Prog. Phys.* 77(7):074601
140. Miles REH, Glerum MWJ, Boyer HC, Walker JS, Dutcher CS, Bzdek BR. 2019. Surface tensions of picoliter droplets with sub-millisecond surface age. *J. Phys. Chem. A* 123(13):3021–29
141. Richards DS, Trobaugh KL, Hajek-Herrera J, Davis RD. 2020. Dual-balance electrodynamic trap as a microanalytical tool for identifying gel transitions and viscous properties of levitated aerosol particles. *Anal. Chem.* 92(4):3086–94
142. Keen S, Yao A, Leach J, Di Leonardo R, Saunter C, et al. 2009. Multipoint viscosity measurements in microfluidic channels using optical tweezers. *Lab Chip* 9(14):2059–62
143. Zhang Y, Wu X, Wang Y, Zhu S, Gao BZ, Yuan XC. 2014. Measurement of the microscopic viscosities of microfluids with a dynamic optical tweezers system. *Laser Phys.* 24(6):5
144. Narayan S, Metaxas AE, Bachnak R, Neumiller T, Dutcher CS. 2020. Zooming in on the role of surfactants in droplet coalescence at the macroscale and microscale. *Curr. Opin. Colloid Interface Sci.* 50:101385
145. Narayan S, Metaxas AE, Bachnak R, Neumiller T, Dutcher CS. 2020. Insights into the microscale coalescence behavior of surfactant-stabilized droplets using a microfluidic hydrodynamic trap. *Langmuir* 36:9827–42
146. Madou MJ. 2002. *Fundamentals of Microfabrication: The Science of Miniaturization*. Boca Raton, FL: CRC Press
147. Goodwin ARH, Donzier EP, Vancauwenberghe O, Fitt AD, Ronaldson KA, et al. 2006. A vibrating edge supported plate, fabricated by the methods of micro electro mechanical system for the simultaneous measurement of density and viscosity: results for methylbenzene and octane at temperatures between (323 and 423) K and pressures in the range (0.1 to 68) MPa. *J. Chem. Eng. Data* 51(1):190–208
148. Etchart I, Chen H, Dryden P, Jundt J, Harrison C, et al. 2008. MEMS sensors for density-viscosity sensing in a low-flow microfluidic environment. *Sens. Actuators A Phys.* 141(2):266–75
149. Cerimovic S, Beigelbeck R, Antlinger H, Schalko J, Jakoby B, Keplinger F. 2012. Sensing viscosity and density of glycerol-water mixtures utilizing a suspended plate MEMS resonator. *Microsyst. Technol.* 18:1045–56
150. Yang LJ, Liu KC, Lin WC. 2014. On deriving surface tension force in MEMS. *J. Appl. Sci. Eng.* 17(3):223–30
151. Arenas KJL, Schill SR, Malla A, Hudson PK. 2012. Deliquescence phase transition measurements by quartz crystal microbalance frequency shifts. *J. Phys. Chem. A* 116(29):7658–67
152. Schuttlefield J, Al-Hosney H, Zachariah A, Grassian VH. 2007. Attenuated total reflection Fourier transform infrared spectroscopy to investigate water uptake and phase transitions in atmospherically relevant particles. *Appl. Spectrosc.* 61(3):283–92

Annual Review of
Physical Chemistry
Volume 72, 2021

Contents

Errata

An online log of corrections to *Annual Review of Physical Chemistry* articles may be found at http://www.annualreviews.org/errata/physchem